Quantitative non-destructive single-frequency thermal-wave-radar imaging of case depths in hardened steels

Y. Wei, A. Melnikov, M. Wang, and (iD) A. Mandelis

View Online   Export Citation   CrossMark

ARTICLES YOU MAY BE INTERESTED IN

AIP Publishing

Quantitative non-destructive single-frequency thermal-wave-radar imaging of case depths in hardened steels

View Online Export Citation CrossMark

Y. Wei,[1,2] A. Melnikov,[1] M. Wang,[1,3,4] and A. Mandelis[1,a]

AFFILIATIONS

[1]Center for Advanced Diffusion-Wave and Photoacoustic Technologies (CADIPT), Department of Mechanical and Industrial Engineering, University of Toronto, Toronto M5S 3G8, Canada
[2]Department of Astronautical Science and Mechanics, Harbin Institute of Technology, Harbin 150001, China
[3]School of Optoelectronic Science and Engineering and Collaborative Innovation Center of Suzhou Nano Science and Technology, Soochow University, Suzhou 215006, China
[4]Key Lab of Advanced Optical Manufacturing Technologies of Jiangsu Province and Key Lab of Modern Optical Technologies of Education Ministry of China, Soochow University, Suzhou 215006, China

[a]Author to whom correspondence should be addressed: mandelis@mie.utoronto.ca

ABSTRACT

Single-frequency thermal-wave radar (SF-TWR) imaging was used to produce dynamic images of effective case depths from phase image frequency scans in AISI 9310 and Pyrowear 53 steels. SF-TWR, as a fast non-destructive testing technique, was also compared with conventional photothermal radiometry measurements in these two types of steel samples using a three-layer theoretical thermal-wave model. In this paper, a novel approach of SF-TWR imaging, combining a three-distinct-layer thermal-wave model and radial phase profiles to image mean value case depths and their lateral non-uniform distributions, yielded quantitative images of case depths in the two hardened steels and exhibited very good correlation with standard Vickers measurements. The SF-TWR images further revealed strong inhomogeneities in the case depth thickness profiles to be used as important feedback to the heat treating manufacturing industry toward the optimization of their case depth hardening process.

Published under license by AIP Publishing. https://doi.org/10.1063/1.5139643

I. INTRODUCTION

Non-destructive and accurate case depth measurements in manufactured metals like steels are important for assessing the heat treating and hardening process. State-of-the-art industrial hardness measurement methods are typically destructive and time-consuming, based on indenter hardness profiles. Many non-destructive techniques are widely applied to detect defects and damage in manufacturing materials, monitor the surface structure, and measure the surface temperature of samples.[1-4] Photothermal radiometry (PTR) was first reported in 1979[5] as a non-contact and non-destructive testing (NDT) technique. It was originally used for the measurement of optical parameters of materials and was further developed to measure thermophysical parameters such as thermal conductivity and thermal diffusivity, case depths, and coating thicknesses.[6-12] Lock-in thermography (LIT) extended the PTR capabilities into the imaging domain.[13-15] However, LIT at fixed modulation frequency is a depth integrated methodology limited to a thermal diffusion length below the surface of industrial solids (steels), giving rise to images that are averages over ∼1–1.5 thermal diffusion lengths weighed by the spatial decay envelope of the oscillating temperature. The thermal diffusion length is also a limitation in its use for quantitative subsurface defect analysis. LIT images are further limited by undersampling at high frequencies due to low camera frame rate limitations. Undersampling usually results in a poor signal-to-noise ratio (SNR) and poor image quality from regions close to the material surface. A high SNR is important for obtaining reliable hardness images. An alternative methodology, the thermal-wave radar (TWR), was introduced to

address sensitivity to subsurface defects/discontinuities and solve the limitations in both PTR and LIT.[16–18] The TWR features linear frequency modulation (LFM) chirps and uses cross correlation (CC) pulse compression and matched filtering to process the signal, a methodology introduced to the photothermal field in 1986.[19–21] Variants of this methodology have also been reported for NDI applications.[22,23] In matched filtering, the chirped modulation is used to compress the energy imparted by the chirp to a narrow correlation peak, which can yield images with maximum SNR. Theoretical and experimental results verified the effectiveness of enhanced SNR and depth resolution of the TWR imaging technique compared to conventional LIT imaging.[18] Very recently, the single-frequency thermal-wave radar (SF-TWR) was introduced as a special case of the TWR imaging modality that was presented as a practical solution for fast imaging requirements from existing thermal cameras so that near surface structures and defects can be quantified for non-destructive imaging (NDI) applications that require high speed performance.[24] In SF-TWR imaging (SF-TWRI), the starting and ending frequencies of a linear frequency modulation sweep are chosen to coincide. There is no "radar" (multi-frequency LFM) signal processing in the excitation waveform of the SF-TWR; however, the TWR algorithm is used, which also works with single-frequency (SF) excitation signals; therefore, the signal processing method was also called SF-TWR. The SF-TWR algorithm enhances subtle changes in thermal phase contrast at fixed modulation frequency. Specifically, in the SF-TWR imaging modality, the TWR algorithm is used instead of conventional LIT algorithms in order to improve the SNR of thermal-wave phases computed with a single-frequency modulated signal acquired within short times, as required for high-frequency/shallow depth imaging when the maximum available camera frame rate is too slow to keep up with the requirements of the sampling theorem. Thermal-wave phases processed with a lock-in algorithm from thermal-diffusion-depth-integrated sample responses at fixed modulation frequency are the preferred signal channel for extracting quantitative parameter measurements from diffusion-wave-based mathematical models. The larger (~3%) LIT phase measurement error at high frequencies, inherent in the time-domain (under)sampling process used with this modality, compared to ~0.3% of TWR phase error, is detrimental to producing accurate parameter values and suitable quantitative image reconstructions. At low frequencies, LIT and TWR algorithms exhibit similar SNR because LIT oversampling at, or near, full camera sampling capacity can produce large numbers of data points over a modulation cycle to match the TWR advantage. However, LIT fares poorly at high frequencies, while quantitative best fits of pixel frequency responses to thermal-wave theory require high SNR throughout the full frequency range of interest, especially at the high end when thermal-wave SNR is already compromised due to the $1/\sqrt{f}$ dependence of the signal. Therefore, the TWR imaging algorithm was extended by introducing the SF-TWR modality at *any* fixed frequency from test samples that exhibit low contrast in thermal-wave phase images, by exploiting the same multi-frequency TWR frequency-domain processing algorithm that suppresses the large measurement error. In SF-TWR, the CC spectrum is computed using the thermal-wave response and excitation signals.[24] In the processing of the TWR algorithm, it does not matter how many frequencies constitute the excitation signal:

It only measures the correlation between the response and excitation signals and reveals important CC peaks. In the algorithm, only the highest-amplitude peak location is tracked and used to extract the corresponding phase value. Because of it, the TWR algorithm works even if a single-frequency component exists in the excitation signal.

Using the highest available camera frame rate regardless of the modulation frequency, SF-TWRI leads to an increased number of sampled points along the modulation waveform compared to conventional LIT imaging. The SF-TWR CC signal generation process is applied to each and every pixel of the camera and is *not* limited by undersampling at high frequencies.[24] This leads to a large reduction in measurement time and higher signal-to-noise ratio across wide frequency ranges, yielding superior image quality especially at high modulation frequencies such as those required to image thin surface layers.

In summary, the SF-TWR represents a next-generation thermography method for imaging important classes of thin layers, materials, and components that require high-frequency thermal-wave probing well above today's available infrared camera technology frame rates. The technique was applied to imaging the thickness of coatings on two different substrates.[24] In contrast, hardened layers and case depths are significantly more challenging because, besides their significantly non-uniform lateral distributions revealed in the present investigation, they also feature continuously variable depth distributions of thermal parameters and can thus only be characterized by an effective case depth. To avoid the complexity of the complete inverse problem, this paper describes the introduction of an optimal method combining a three-distinct-layer thermal-wave model and radial phase profiles to image mean value case depths and their lateral non-uniform distributions. The model was validated through good correlations with destructive case depths in the two investigated steels.

II. MATERIALS AND METODS

A. PTR and SF-TWR experimental setups

The PTR and SF-TWR systems were incorporated in the same experimental architecture to facilitate quantitative thermal-wave measurements under identical conditions. The PTR system is shown in Fig. 1. It consists of a laser excitation source, modulator, and signal acquisition and detection processing parts. A semiconductor laser (Model JOLD-45-CPXF-1L) was used as the light source emitting at 808 nm. A function generator was employed to modulate the laser intensity. The laser beam was collimated, homogenized, and spread by a microlens array across the imaged area. When the sample was optically excited, the diffuse blackbody radiation thus generated at a particular coordinate location was directed to a pair of off-axis paraboloidal mirrors. An infrared detector (Model PVI-4TE-5, VIGO systems) was placed at the focus of the receiving paraboloidal mirror that captured the infrared signal of the sample coordinate location after collection and collimation by the first focused mirror. The detected signal was demodulated by a lock-in amplifier, and the data were stored in a computer.

The SF-TWR detection system is shown in Fig. 2. It also consists of the same laser excitation source, a modulation and signal/
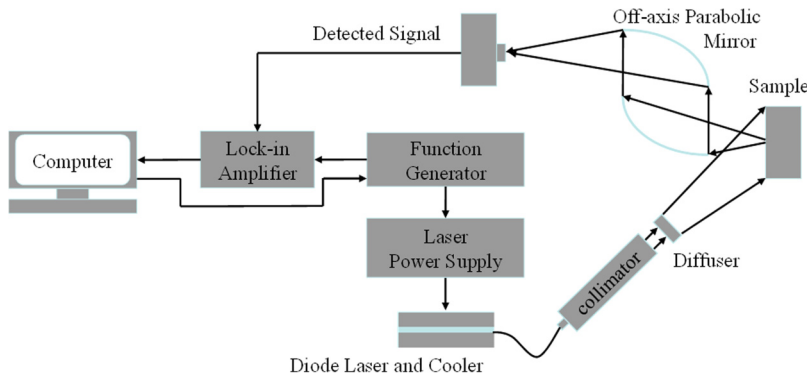
FIG. 1. Diagram of the PTR system.

image processing sub-system. The modulated signal was generated by a computerized data acquisition card (USB-6229) controlling the laser output waveform. Image information was collected directly by a mid-infrared (MIR) camera (CEDIP Titanium model 520 M).

The signal generated by the data acquisition card was collected and processed using an in-house developed algorithm implemented in Labview. Details of the SF-TWR signal processing computations can be found in Ref. 24.

B. Materials and theoretical model

Two kinds of gear-tooth shaped steel sample types were investigated, AISI 9310 and Pyrowear 53. These materials are widely used as aviation components, combustion engines, automotive transmissions, and general machinery. Two AISI 9310 samples were labeled A11 and A_{ref}, while another two Pyrowear 53 samples were labeled P6 and P_{ref}. A_{ref} and P_{ref} represented the associated unhardened reference samples, which were used to normalize the phases of A11 and P6, respectively. The imaged areas of A11 and P6 are shown in Figs. 3(a) and 3(b), respectively.

Their effective case depths measured by the conventional destructive indenter method were 1.05 mm and 1.46 mm, separately. The samples were cleaned before the measurements and were placed on the TW imager sample holder for irradiation with the expanded laser beam.

The geometry of the one-dimensional three-layer model is shown in Fig. 4. The three-layer model was chosen as a close approximation to the variable case depth. It substituted three

discrete layers for the continuously variable hardness profile, representing the surface roughness layer, the hardened layer, and the semi-infinite layer.

The thermal-wave signal from the sample surface, $\Delta T_{1N}(0, f)$, normalized with the signal from a semi-infinite layer with the substrate properties, can be written as[25]

$$\Delta T_{1N}(0, f) = b_{31} \frac{(1 - R_1)(1 - \gamma_{01})}{(1 - R_s)(1 - \gamma_{03})} \left(\frac{1 + \rho_{321} e^{-2(1+i)\sqrt{\pi f Q_1}}}{1 - \rho_{321} e^{-2(1+i)\sqrt{\pi f Q_1}}} \right), \quad (1)$$

where $Q_m = \frac{L_m}{\sqrt{\alpha_m}}$, $\gamma_{mn} = \frac{b_{mn}-1}{b_{mn}+1}$, $b_{mn} = \frac{P_m}{P_n}$, $P_m = \frac{k_m}{\sqrt{\alpha_m}}$, and $\rho_{321} = -\gamma_{21} \left[\frac{1+(\gamma_{32}/\gamma_{21})e^{-2(1+i)\sqrt{\pi f Q_2}}}{1+(\gamma_{32}\gamma_{21})e^{-2(1+i)\sqrt{\pi f Q_2}}} \right]$, $m, n = 0, 1, 2, 3$ stands for air, roughness layer, hardened layer, and substrate, respectively. L_m is the thickness of the various layers (roughness and hardened layer), and α_m and k_m are the thermal diffusivity and conductivity of the corresponding layer, respectively. Q_m and P_m are composite transport parameters appearing in thermal-wave layer models. R_1 is the reflectivity of the roughness layer and R_s is that of the substrate.

In Eq. (1), $Q_2 = \frac{L_2}{\sqrt{\alpha_2}}$ represents a combined thermal-wave transport parameter to which the photothermal signal is most highly sensitive, and thus its measurement is most reliable through best fitting of the theory to the frequency-scanned data. It should be mentioned that lateral inhomogeneities of the case hardened sample lead to 3D heat flow even with homogeneous surface heating sources. This may limit the effective lateral resolution to the order of the thermal diffusion length when using a three-layer 1D model. It is well-known that lateral resolution can improve using higher frequency images.

III. DISCUSSION AND RESULTS

A. Sample A11

SF-TWR images of samples A11 and P6 were obtained at various modulation frequencies, one at a time. The phase images of sample A11 at three frequencies, 1 Hz, 5 Hz, and 10 Hz, are shown in Fig. 5. The amplitude is influenced by the surface optical properties of the samples, while the phase exhibits a purely thermal-wave response independent of surface optical variations and
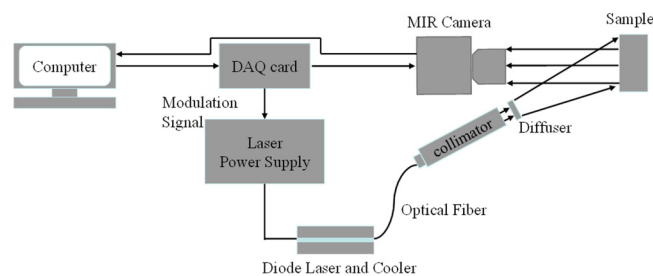

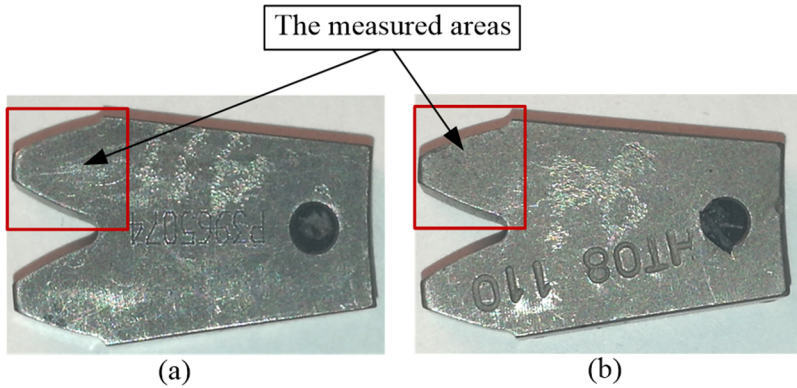**FIG. 2.** Diagram of the SF-TWR system.

FIG. 3. The imaged areas of two gear-tooth steel samples: (a) sample A11; (b) sample P6.

inhomogeneities. For this reason, in this paper, the phase was selected as the only thermal-wave signal channel.

The quantification of the thermophysical parameters was obtained by fitting the experimental data to the theoretical model. The frequency dependence of one pixel, named "pixel D," was chosen to compare the SF-TWR and PTR results. The experimental data of each pixel were fitted according to the three-layer theoretical model in Eq. (1). The sample A_{ref} was used to normalize the SF-TWR and PTR signals from sample A11 under identical experimental conditions. The A11 normalized SF-TWR and PTR pixel D phase dependencies on frequency are shown in Figs. 6(a) and 6(b). Both SF-TWR and PTR experimental data were fitted well by the three-layer theoretical model.

The parameter Q_2 exhibits an exponential dependence on the signal and thus high sensitivity, which results in excellent reliability. The fminsearchbnd solver[26] was used to minimize the sum of the squares of errors between the experimental and calculated data starting with an initial estimate within a fixed interval. With this program, different starting points in the range of 0–1 s$^{1/2}$ deliver

different results of the theoretical curve best-fitted to the experimental points. In this manner, the mean value of parameter Q_2 and its standard deviation (StD), a measure of the scatter of the best-fitted results, were determined. The best fits were used to verify the accuracy of the fitted parameters. The reliability/ uniqueness of the fitted parameters to the thermal-wave mathematical model is a key element of quantitative SF-TWR imaging in which the entire frequency response of each pixel dependence is fitted separately while non-uniqueness may lead to parameter image reliability issues. Measurement precision is characterized by the image noise in case of pixel spatial resolution less than the lateral inhomogeneity or the frequency dependent diffusion length limitation. The parameter Q_2 was found to be $0.3 \pm 1.9 \times 10^{-4} s^{0.5}$ using SF-TWRI and $0.31 \pm 4.20 \times 10^{-6} s^{0.5}$ using PTR. Clearly, these numbers are very close and show the consistency of the two methodologies. The low standard deviations (StD) confirm the reliability of the evaluated parameter Q_2. Although the shapes of pixel and single detector (SD) frequency dependence curves are different, that may be caused by higher noise levels in camera measurements than the SD and non-negligible frequency response sensitivity to surface roughness which would tend to heterogenize responses of camera pixel groups (around 40μm) at different locations. This type of coordinate-based variation is not easily captured in single detector PTR measurements. Using the three-layer model with the highly sensitive to case depth parameter Q_2 allows a significant reduction of these in-plane geometric factors and leads to measurements in close agreement between the two methods. Other (secondary) parameters were not used for estimating the case depth, as their relative weight and thus significance in the measurement of the primary parameter (case depth) were minimal.

The image of the Q_2 parameter derived as the best-fitted result of the pixel frequency response to SF-TWR is shown in Fig. 7(a). It should be mentioned that lateral resolution is also limited by the pixel size.

To transform the Q_2 parameter to effective case depth, the value of the thermal diffusivity, α, was required. To measure α, phase images of the sample A_{ref} and A11 were obtained with focused laser beam at three frequencies (2 Hz, 5 Hz, and 10 Hz) (Fig. 8).
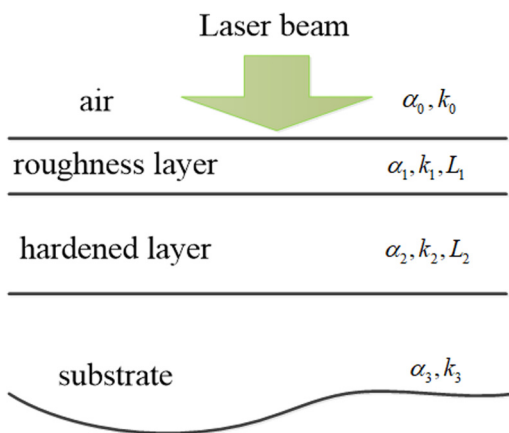

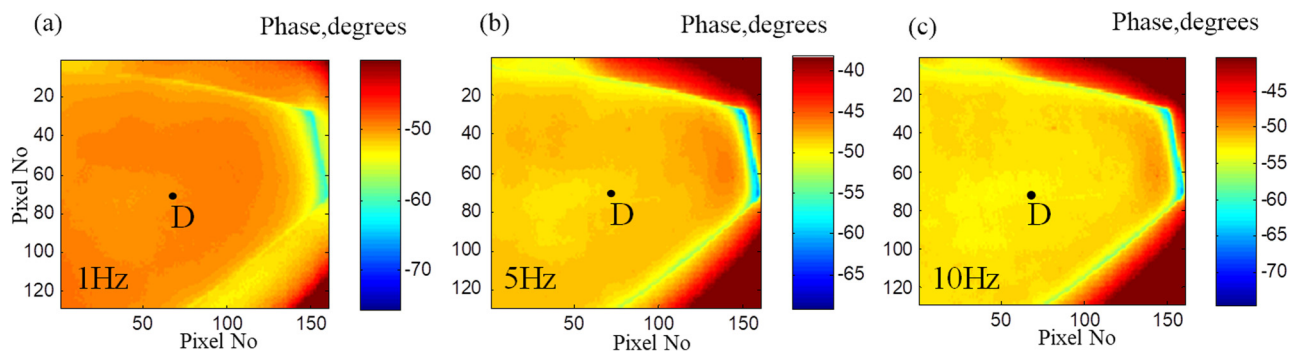**FIG. 4.** A one-dimensional three-layer thermal-wave model geometry.

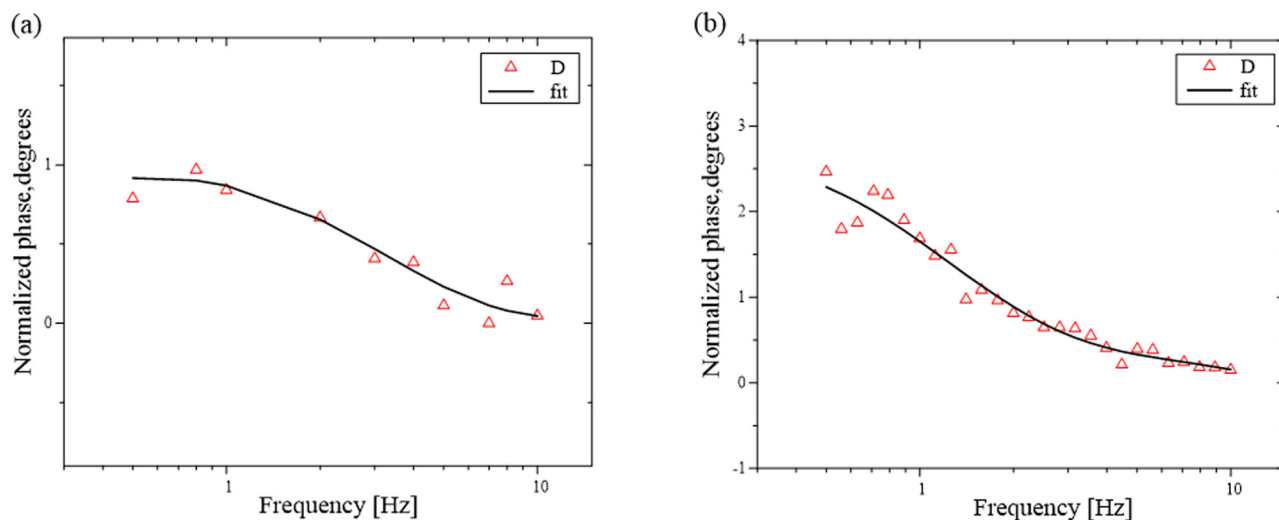**FIG. 5.** Phase images of sample A11 with its own substrate as reference: (a) 1 Hz; (b) 5 Hz; (c) 10 Hz.

FIG. 6. Normalized phase of sample A11 dependence on frequency and best fits of pixel D in Fig. 5: (a) the best-fitted parameter Q_2 was $0.3\,s^{0.5}$ for SF-TWRI. (b) Q_2 was $0.31\,s^{0.5}$ for PTR.
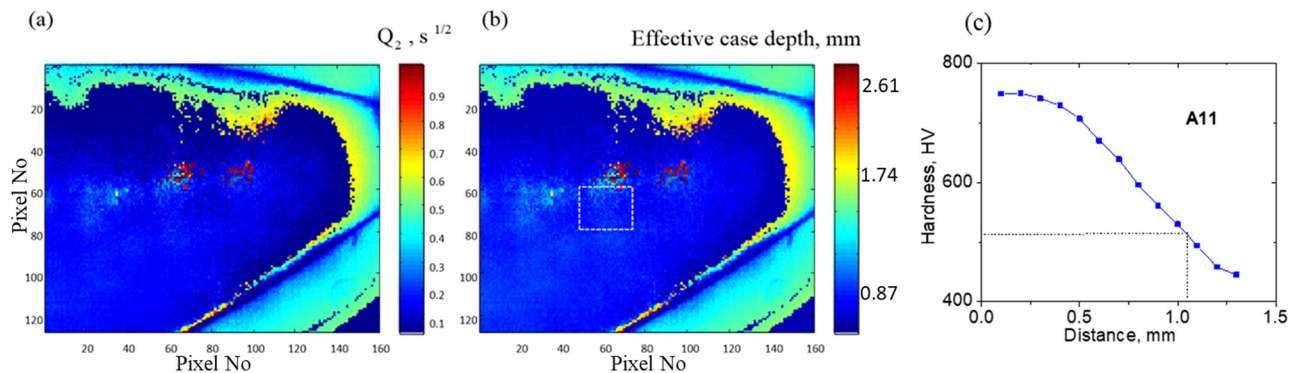

FIG. 7. Sample A11: (a) the fitted Q_2 parameter image; (b) the constructed quantitative case depth image; (c) Vickers hardness profile. The average effective case depth of the highlighted area is 0.93 mm; the case depth according to the Vickers measurement is 1.05 mm.
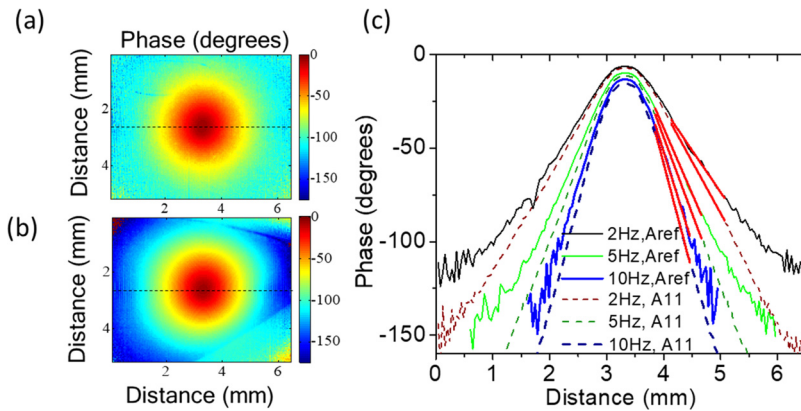
FIG. 8. Phase images of A_{ref} (a) and A11 (b) at 2 Hz and lateral (radial) phase profiles of A_{ref} and A11 (c) at three frequencies along the horizontal line in (a) and (b). The linear parts of radial phase distributions were used for estimating the phase slopes used for fitting to Eq. (2).

The SF-TWR lateral (radial) profile phase measurements at all three frequencies are shown in Fig. 8(b). α of the hardened layer in sample A11 and of the reference sample A_{ref}, the latter representing the unhardened bulk of A11, were calculated from the slopes of the lateral phase profiles in Fig. 8(b) using Eq. (2),[27] along the chosen horizontal line in Figs. 8(a) and 8(b),

$$\alpha = \frac{\pi f}{s^2}, \qquad (2)$$

where s is the slope of the linear portion of the phase radial distribution and f is the laser modulation frequency. The phase slope values at 5 and 10 Hz are shown in Table I. The diffusivity values at these frequencies, calculated according to Eq. (2), are also shown in Table I. It is seen that diffusivity variations of the reference sample with frequency are negligible (within statistical error). The averaged diffusivity of the three frequencies is $\alpha = 10.5 \times 10^{-6}\,\text{m}^2/\text{s}$ for the reference sample (substrate). It should be mentioned that the estimated substrate diffusivity ($10.5 \times 10^{-6}\,\text{m}^2/\text{s}$) is in excellent agreement with the value range $9.42 \times 10^{-6} - 13.8 \times 10^{-6}\,\text{m}^2/\text{s}$ calculated according to $\alpha = k/\rho c_p$ from published AISI 9310 steel data,[10,28] where ρ is the density and c_p is the specific heat capacity. The diffusivity of the A11 hardened layer is less than that of the unhardened reference sample, A_{ref}, which is consistent with previously observed diffusivity decreases in hardened steels.[11,29–31]

The inhomogeneous hardness depth distribution requires reliable diffusivity measurements to be made at high frequencies

in the thermally thick range.[25] At 10 and 5 Hz modulation frequencies, the A11 radial profile slopes in Fig. 8(c) yield $\alpha = 7.9 \pm 0.1\,\text{mm}^2/\text{s}$ and $7.7 \pm 0.1\,\text{mm}^2/\text{s}$, leading to thermal diffusion length, $\mu(f) = \sqrt{\alpha/\pi f}$, values ~0.5 mm and 0.7 mm, respectively, well within the extent of the hardened layer [Fig. 7(c)]. The foregoing thermal diffusivity values at 2 Hz yielded a thermal diffusion length of 1.12 mm. In view of the hardness profile of Fig. 7(c), this reaches the hardened layer boundary and cannot be used for a reliable estimate of α in the hardened layer. The 2-Hz radial slope in Fig. 8(c) yielded $\alpha < 7.7\,\text{mm}^2/\text{s}$. This is the result of neglecting the effects of the thermal-wave reflection-like denominator term of ρ_{321} in Eq. (1), which decreases the value of ρ_{321} by increasing the value of Q_2 in the exponent of $e^{-2(i+1)\sqrt{\pi f Q_2}}$ thereby effectively decreasing the value of α. This term is negligible at higher frequencies in the thermally thick range. Furthermore, the hardness profile and the corresponding diffusivity profile may vary in different regions of the sample surface. This can be a complication in the estimation of local case depths. In any case, the difference in diffusivities between the reference and case hardened layers was consistently found to be on the order of $25 \pm 3\%$ for 10 Hz thermal-wave probing as shown in Table I and also as measured at random locations across the hardened sample A11. Therefore, an optimal estimate of the diffusivity of the hardened layer across the sample was taken to be $7.9\,\text{mm}^2/\text{s}$ (75% of the value of the substrate diffusivity). This approximation allows the use of literature thermal diffusivity values of the unhardened layer, thereby avoiding the more time-consuming, yet feasible, diffusivity measurements at each point across the sample surface. The diffusivity $7.9\,\text{mm}^2/\text{s}$ was further used to construct the quantitative case depth image shown in Fig. 7(b). To validate the SF-TWR results, the case depth was also measured using a Vickers hardness tester [Fig. 7(c)]. The value 1.05 mm measured with the tester is close to the average value of the highlighted square area in Fig. 7(b) (0.93 mm) measured by SF-TWR. The observed difference of 11% may be caused by the discrete layer approximation used in the PTR method in lieu of the continuously variable diffusivity depth profile exhibited from the Vickers hardness profile. It should be mentioned

TABLE I. The phase slopes and calculated diffusivity values of samples A_{ref} and A11 at two thermally thick frequencies.

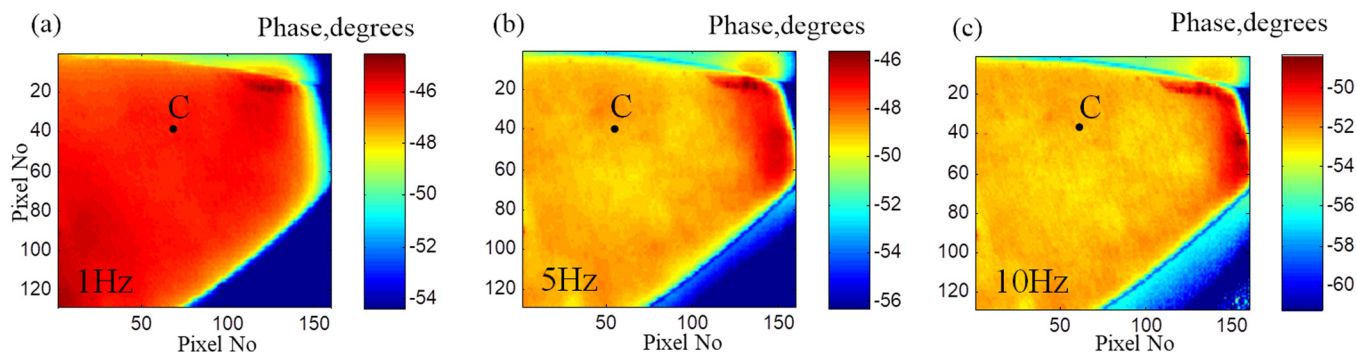| f	A_{ref}		A11	
	Phase slope, s (degree/mm)	α (mm²/s)	Phase slope, s (degree/mm)	α (mm²/s)
5 Hz	-70.4 ± 0.5	10.4 ± 0.2	-81.7 ± 0.5	7.7 ± 0.1
10 Hz	-97.7 ± 1.9	10.8 ± 0.4	-115.1 ± 0.8	7.9 ± 0.1

FIG. 9. Phase images of sample P6 with its own substrate as reference: (a) 1 Hz; (b) 5 Hz; (c) 10 Hz.

that statistical analysis of nine neighboring pixels in the highlighted area showed a StD of 4%–10%.

B. Sample P6

The phase images of the other sample P6 at the same three frequencies (1 Hz, 5 Hz, and 10 Hz) are shown in Fig. 9. Like sample A11, the SF-TWR frequency dependence of one pixel called "Pixel C" was chosen to compare with the PTR results. Sample P_{ref} was used to normalize the SF-TWR and PTR signals from sample P6 under the same experimental conditions. Figure 10 shows the best fits of both SF-TWR and PTR experimental data to the theory

according to Eq. (1). The SF-TWRI best-fitted parameter value $Q_2 = 0.46\,s^{0.5}$ is very close to that measured from PTR, $Q_2 = 0.46\,s^{0.5}$.

The Q_2 parameter image derived as the best-fitted result of the pixel frequency response to SF-TWR is shown in Fig. 11(a). The corresponding case depth image, presented in Fig. 11(b), was calculated using the measured diffusivity. The focused-beam phase images of sample P_{ref} and P6 at 2 Hz, used for diffusivity estimation, are shown in Figs. 12(a) and 12(b). Figure 12(c) shows the lateral (radial) phase profiles at the three frequencies along the chosen horizontal line in Figs. 12(a) and 12(b).
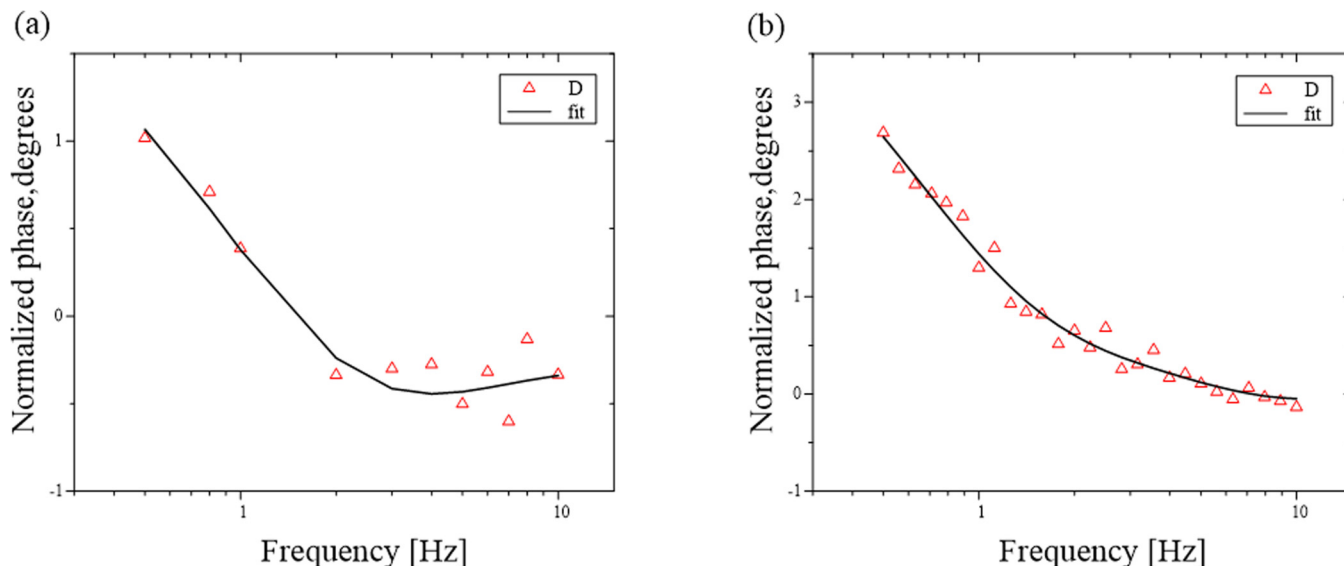

FIG. 10. Normalized phase of sample P6 dependence on frequency, and best fits to Eq. (1). (a) The SF-TWRI pixel C best-fitted parameter was $Q_2 = 0.46\,s^{0.5}$. (b) The PTR fitted parameter Q_2 was also measured to be $0.46 \times 10^{-6}\,s^{0.5}$.
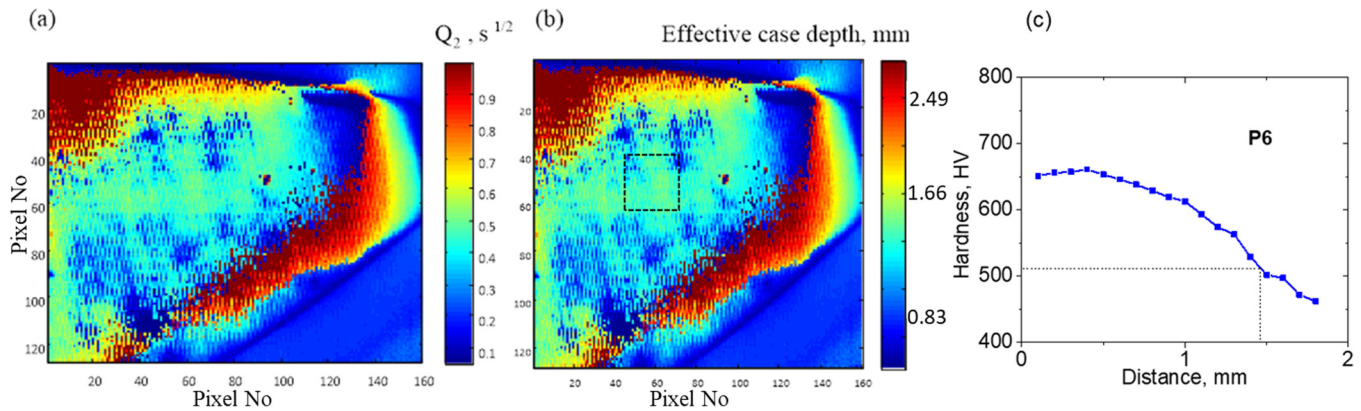
FIG. 11. Sample P6: (a) the best-fitted Q_2 parameter image; (b) the constructed quantitative case depth image; (c) Vickers hardness profile. The average effective case depth of the highlighted area is 1.18 mm; the case depth according to the Vickers measurement is 1.46 mm.

The diffusivity α was calculated using Eq. (2) and the linear ranges of the detailed lateral (radial) phases (Fig. 12). The phase slopes and calculated diffusivities at 5 Hz and 10 Hz are shown in Table II. As expected, the diffusivity of the reference sample remains unchanged with frequency within statistical error and the average value was found to be $\alpha = 10.1 \times 10^{-6}$ m^2/s for P_{ref}.

Similar to the previous sample, the hardened layer exhibits lower diffusivity than the substrate. The thermal diffusion lengths in the hardened sample at 5 and 10 Hz are ~0.7 and 0.5 mm, respectively, satisfying the thermally thick condition well within the hardened layer thickness [Fig. 11(c)], which allows using the average value of diffusivity 8.1 mm^2/s of the hardened layer for case depth calculations. The thermal diffusion length at 2 Hz was calculated to be 1.14 mm, which was excluded from the estimation of the thermal diffusivity of the hardened P6 layer as not entirely in the thermally thick range. As in the A11 case, the 2-Hz radial slope of Fig. 12(c) gave a smaller diffusivity value than the 5-Hz and 10-Hz slopes, consistent with the approximation used

without the reflection-like denominator in the term ρ_{321} in Eq. (1). The diffusivity of P6 was found to be ca. $80 \pm 1\%$ of the substrate diffusivity for this kind of steel. The calculated value of the substrate diffusivity is higher than that (7.06×10^{-6} m^2/s) calculated from the only available open literature specification data (conductivity, density, and specific heat) by a steel manufacturer.[32] It is evident that the scarcity of alternative literature values makes it hard to establish a measurement range and detailed information on the microscopic structure of the measured P6 and make comparison with independent measurements. The case depth image thus obtained is shown in Fig. 11(b). To validate the SF-TWR results, the case depth was also measured using the Vickers hardness tester. The difference between the directly measured value (1.46 mm) [Fig. 11(c)] and the average value in the highlighted square area (1.19 mm) was found to be 18%, which may be caused by lateral hardness inhomogeneity. A StD analysis of nine neighboring pixels in the highlighted area yielded StD of 3%–14%.
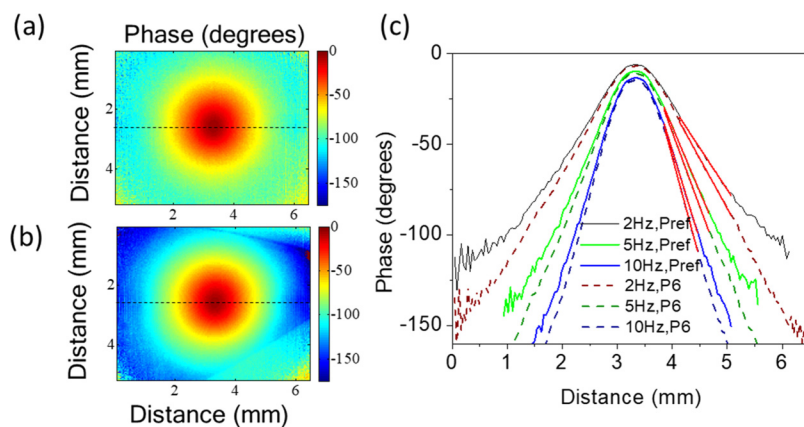

FIG. 12. Phase images of P_{ref} (a) and P6 (b) at 2 Hz and lateral (radial) phase profiles (c) at three frequencies along the horizontal line in (a) and (b). The linear parts of radial phase distributions were used for estimating the phase slopes.

TABLE II. The phase slopes and diffusivities of samples P$_{ref}$ and P6 at two thermally thick frequencies.

	P$_{ref}$		P6	
f	Phase slope, s (deg/mm)	α (mm^2/s)	Phase slope, s (deg/mm)	α (mm^2/s)
5 Hz	-71.7 ± 0.5	10 ± 0.1	-82.2 ± 0.5	7.6 ± 0.1
10 Hz	-98.7 ± 0.5	10.6 ± 0.1	-112.8 ± 0.9	8.1 ± 0.1

IV. CONCLUSIONS

Single-frequency thermal-wave radar (SF-TWR) measurements were used to produce quantitative images of the effective case depth of two types of hardened steels and to compare the results with conventional PTR measurements. The experimental frequency response data of selected camera pixels were best-fitted to a three-layer theoretical model and the parameter $Q_2 = \frac{L_2}{\sqrt{\alpha_2}}$ was extracted. Both SF-TWR and PTR Q_2 parameters were found to be in close agreement with each other for both steel types/samples, thereby demonstrating the reliability of quantitative non-destructive SF-TWR imaging of hardness case depths in industrial steels. It was shown that using the value of diffusivity of the hardened layer obtained at frequencies in the thermally thick range allows the quantitative conversion of the Q_2 image into a case depth image.

ACKNOWLEDGMENTS

DATA AVAILABILITY

Data available on request from the authors.

REFERENCES

[1]C. C. H. Lo, E. R. Kinser, and Y. Melikhov, "Magnetic nondestructive characterization of case depth in surface-hardened steel components," AIP Conf. Proc. **820**, 1253 (2006).

[2]W. Morgner and F. Michel, "Some new results in the field of non-destructive case depth measuring," *9th European NDT Conference (ECNDT 2006), Berlin, Germany, 25–29 September* (NDTnet, 2006).

[3]J. C. Krapez and R. L. I. Voti, "Effusivity depth profiling from pulsed radiometry data: Comparison of different reconstruction algorithms," Anal. Sci. **17**, 417 (2001).

[4]C. Wang and A. Mandelis, "Case depth determination in heat-treated industrial steel products using photothermal radiometric interferometric phase minima," NDT&E Int. **40**, 158 (2007).

[5]P. E. Nordal and S. O. Kanstad, "Photothermal radiometry," Phys. Scr. **20**, 659 (1979).

[6]A. C. Tam and B. Sullivan, "Remote sensing applications of pulsed photothermal radiometry," Appl. Phys. Lett. **43**, 333 (1983).

[7]E. Welsch and D. Ristau, "Photothermal measurements on optical thin films," Appl. Opt. **34**, 7239 (1995).

[8]A. Kusiak, J. Martan, J. L. Battaglia, and R. Daniel, "Using pulsed and modulated photothermal radiometry to measure the thermal conductivity of thin films," Thermochim. Acta **556**, 1 (2013).

[9]N. Fleurence, B. Hay, G. Davée, A. Capella, and E. Foulon, "Thermal conductivity measurements of thin films at high temperature modulated photothermal radiometry at LNE," Phys. Status Solidi A **212**, 535 (2015).

[10]X. Guo, K. Sivagurunathan, J. Garcia, A. Mandelis, S. Giunta, and S. Milletari, "Laser photothermal radiometric instrumentation for fast in-line industrial steel hardness inspection and case depth measurements," Appl. Opt. **48**, C11 (2009).

[11]L. Nicolaides, A. Mandelis, and C. J. Beingessner, "Physical mechanisms of thermal diffusivity depth-profile generation in hardened low-alloy Mn, Si, Cr, Mo steel reconstructed by photothermal radiometry," J. Appl. Phys. **89**, 7879 (2001).

[12]A. Mandelis, M. Munidasa, and L. Nicolaides, "Laser infrared photothermal radiometric depth profilometry of steels and its potential in rail track evaluation," NDT&E Int. **32**, 437 (1999).

[13]D. Wu and G. Busse, "Lock-in thermography for nondestructive evaluation of materials," Rev. Gen. Therm. **37**, 693 (1998).

[14]C. Wallbrink, S. A. Wade, and R. Jones, "The effect of size on the quantitative estimation of defect depth in steel structures using lock-in thermography," J. Appl. Phys. **101**, 104907 (2007).

[15]C. Meola, G. M. Carlomagno, A. Squillace, and A. Vitiello, "Non-destructive evaluation of aerospace materials with lock-in thermography," Eng. Failure Anal. **13**, 380 (2006).

[16]R. Velazquez-Hernandez, A. Melnikov, A. Mandelis, K. Sivagurunathan, M. E. Rodriguez-Garcia, and J. Garcia, "Non-destructive measurements of large case depths in hardened steels using the thermal-wave radar," NDT&E Int. **45**, 16 (2012).

[17]N. Tabatabaei, A. Mandelis, and B. T. Amaechi, "Thermophotonic radar imaging: An emissivity normalized modality with advantages over phase lock-in thermography," Appl. Phys. Lett. **98**, 163706 (2011).

[18]N. Tabatabaei and A. Mandelis, "Thermal-wave radar: A novel subsurface imaging modality with extended depth-resolution dynamic range," Rev. Sci. Instrum. **80**, 034902 (2009).

[19]A. Mandelis, "Frequency modulated (FM) time delay photoacoustic and photothermal wave spectroscopies. Technique, instrumentation and detection. Part I: Theoretical," Rev. Sci. Instrum. **57**, 617 (1986).

[20]A. Mandelis, L. M. L. Borm, and J. Tiessinga, "Frequency modulated (FM) time delay photoacoustic and photothermal wave spectroscopies. Technique, instrumentation and detection. Part II: Mirage effect spectrometer design and performance," Rev. Sci. Instrum. **57**, 622 (1986).

[21]A. Mandelis, L. M. L. Borm, and J. Tiessinga, "Frequency modulated (FM) time delay photoacoustic and photothermal wave spectroscopies. Technique, instrumentation and detection. Part III: Mirage effect spectrometer, dynamic range and comparison to pseudo random binary sequence (PRBS) method," Rev. Sci. Instrum. **57**, 630 (1986).

[22]R. Mulaveesala and S. Tuli, "Theory of frequency modulated thermal wave imaging for nondestructive subsurface defect detection," Appl. Phys. Lett. **89**, 191913 (2006).

[23]R. Mulaveesala and S. Venkata Ghali, "Coded excitation for infrared non-destructive testing of carbon fiber reinforced plastics," Rev. Sci. Instrum. **82**, 054902 (2011).

[24]A. Melnikov, L. Chen, D. Ramirez Venegas, K. Sivagurunathan, Q. Sun, A. Mandelis, and I. R. Rodriguez, "Single frequency thermal wave radar: A next-generation dynamic thermography for quantitative non-destructive imaging over wide modulation frequency ranges," Rev. Sci. Instrum. **89**, 044901 (2018).

[25]A. Mandelis, *Diffusion-Wave Fields: Mathematical Methods and Green Functions* (Springer, New York, 2001), Chap. 2.

[26]J. D'Errico, see http://www.mathworks.com/matlabcentral/fileexchange/8277 for fminsearch.

[27]K. Strzałkowski, M. Streza, and M. Pawlak, "Lock-in thermography versus PPE calorimetry for accurate measurements of thermophysical properties of solid samples: A comparative study," Measurement **64**, 64 (2015).

[28]See http://www.doubleeagleagleyalloys.com/products/carbon-alloysproducts/aisi-9310-aircraft-quality/ for Physical properties of AISI 9310.

[29]D. Fournier, J. P. Roger, A. Bellouati, C. Boue, H. Stamm, and F. Lakestani, "Correlation between hardness and thermal diffusivity," Anal. Sci. **17**, 158 (2001).

[30]H. G. Walther, D. Fournier, J. C. Krapez, M. Luukkala, B. Shmitz, C. Sibilia, H. Stamm, and J. Thoen, "Photothermal steel hardness measurements—Results and perspectives," Anal. Sci. **17**, 165 (2001).

[31]K. M. Boubaker, M. Bouhafs, and N. Yacoubi, "A quantitative alternative to the Vickers hardness test based on a correlation between thermal diffusivity and hardness—Applications to laser-hardened carburized steel," NDT&E Int. **36**, 547 (2003).

[32]See https://www.steelgr.com/Steel-Grades/High-Alloy/pyrowear-53.html for Physical Properties of Pyrowear 53.